Theoretical investigation of the design and performance of a dual energy (kV and MV) radiotherapy imager

Langechuan Liu, Larry E. Antonuk,[a] Youcef El-Mohri, Qihua Zhao, and Hao Jiang
Department of Radiation Oncology, University of Michigan, Ann Arbor, Michigan 48109

Purpose: In modern radiotherapy treatment rooms, megavoltage (MV) portal imaging and kilovoltage (kV) cone-beam CT (CBCT) imaging are performed using various active matrix flat-panel imager (AMFPI) designs. To expand the clinical utility of MV and kV imaging, MV AMFPIs incorporating thick, segmented scintillators and, separately, kV imaging using a beam's eye view geometry have been investigated by a number of groups. Motivated by these previous studies, it is of interest to explore to what extent it is possible to preserve the benefits of kV and MV imaging using a single AMFPI design, given the considerably different x ray energy spectra used for kV and MV imaging. In this paper, considerations for the design of such a dual energy imager are explored through examination of the performance of a variety of hypothetical AMFPIs based on x ray converters employing segmented scintillators.
Methods: Contrast, noise, and contrast-to-noise ratio performances were characterized through simulation modeling of CBCT imaging, while modulation transfer function, Swank factor, and signal performance were characterized through simulation modeling of planar imaging. The simulations were based on a previously reported hybrid modeling technique (accounting for both radiation and optical effects), augmented through modeling of electronic additive noise. All designs employed BGO scintillator material with thicknesses ranging from 0.25 to 4 cm and element-to-element pitches ranging from 0.508 to 1.016 mm. A series of studies were performed under both kV and MV imaging conditions to determine the most advantageous imager configuration (involving front or rear x ray illumination and use of a mirror or black reflector), converter design (pitch and thickness), and operating mode (pitch-binning combination).
Results: Under the assumptions of the present study, the most advantageous imager design was found to employ rear illumination of the converter in combination with a black reflector, incorporate a BGO converter with a 0.508 mm pitch and a 2 cm thickness, and operate at full resolution for kV imaging and 2×2 binning mode for MV imaging. Such a dual energy imager design should provide soft tissue visualization at low, clinically practical doses under MV conditions, while helping to preserve the high spatial resolution and high contrast offered by kV imaging.
Conclusions: The authors' theoretical investigation suggests that a dual energy imager capable of largely preserving the desirable characteristics of both kV and MV imaging is feasible. Such an imager, when coupled to a dual energy radiation source, could facilitate simplification of current treatment room imaging systems (as well as their associated quality assurance), and facilitate more precise integration of kV and MV imaging information by virtue of reduced geometric uncertainties. © *2015 American Association of Physicists in Medicine.* [http://dx.doi.org/10.1118/1.4915120]

1. INTRODUCTION

In external beam radiotherapy, the goal of maximizing radiation dose to the tumor, while minimizing dose to surrounding healthy tissues, is assisted through routine use of megavoltage (MV) portal imaging and/or kilovoltage (kV) cone-beam CT (CBCT) imaging in the treatment room. In each case, the imaging detector is typically based on an indirect detection active matrix flat panel imager (AMFPI) which consists of some form of overlying x ray converter coupled to a two-dimensional (2D) pixelated array, each pixel of which contains an amorphous silicon (a-Si:H) photodiode and a thin-film transistor (TFT).[1] Portal imaging is performed using the MV treatment beam and an AMFPI employing a converter taking the form of a thick phosphor screen and a metal plate (e.g., an ~133 mg cm^{-2} Gd$_2$O$_2$S:Tb screen and an ~1 mm copper plate). kV CBCT imaging is performed using a dedicated, independent diagnostic x ray source and an AMFPI employing a converter typically consisting of an ~600 μm CsI:Tl screen.[2] The kV source and imager are mounted to the gantry of the treatment machine, positioned at a 90° rotational offset with respect to the central axis of the treatment beam.

In the context of these widely practiced imaging techniques, it is interesting to note that a number of investigators have

examined the possibility of expanding the clinically useful information that can be obtained from imaging with the treatment beam or a kilovoltage x ray source. For example, the same combination of a treatment beam and a MV AMFPI used for portal imaging can also be employed to perform volumetric imaging (i.e., MV CBCT) which offers several distinct advantages compared to kV CBCT. These include the reduction of streak artifacts caused by metal implants[3] and the ready applicability of MV CT numbers for treatment planning dose calculations.[4] However, conventional MV AMFPIs suffer from very low x ray quantum efficiency (QE) and, as a result, very low detective quantum efficiency (~2% and 1% at 6 MV, respectively),[5] necessitating the use of relatively high imaging doses (e.g., ~50–200 cGy) in order to achieve soft tissue visualization using MV CBCT.[6,7] To address this challenge, various approaches for increasing the QE of MV imagers have been investigated or implemented, such as xenon gas ion chambers arranged in a fan-beam geometry,[8] and thick, segmented scintillating crystals arranged in the form of a linear array[9–12] or a 2D matrix.[13–24] In particular, the approach involving a 2D matrix of segmented scintillator elements (based on CsI:Tl, $Bi_4Ge_3O_{12}$ [BGO], or $Lu_{1.8}Y_{0.2}SiO_5$ [LYSO]) has been explored both theoretically and empirically.[17–24] Based on this approach, one prototype employing ~1.13 cm thick BGO crystals has demonstrated DQE values as high as ~20%—representing an ~20-fold increase compared with that of conventional MV AMFPIs.[19] Such a large increase in DQE has been shown to enable the acquisition of high quality MV CBCT images at a total dose as low as ~4 cGy (Ref. 21)—an amount comparable to that required to obtain a single portal image from a conventional MV AMFPI.[1]

Expansion of the clinical utility of kV CBCT can be achieved through use of a beam's eye view (BEV) geometry in which the diagnostic source is positioned so as to provide the same radiation field of view (FOV) as that of the treatment source. Such BEV kV imaging has been investigated using different approaches: through the integration of an additional kV source in the treatment head,[25–27] and through modification of the treatment beam line so as to increase the low energy component of the beam.[28–32] The latter approach has been explored through the use of a low-Z target,[28–30] a modified linear accelerator waveguide,[31] or reduction of the electron beam energy.[32] Compared with the current kV CBCT imaging which is performed with the aforementioned rotational offset of the kV source relative to the MV source, BEV kV imaging would eliminate the geometric uncertainties associated with that offset and the need for additional quality assurance effort to ensure the coincidence of the isocenters of the kV and MV radiation fields, while preserving the superior contrast of images compared to that obtained using the MV treatment beam. BEV kV imaging could also enhance the effectiveness of tumor tracking[33] in a near real-time mode. Furthermore, the coincidence of the kV and MV FOVs would facilitate reconstruction of images with the complementary strengths of kV and MV imaging, such as superior contrast-to-noise ratio (CNR) and reduced metal artifacts, respectively. (Note that CBCT imaging based on a combination of kV and MV image acquisitions has been explored with a conventional, orthogonally mounted kV system.)[34]

Given the considerably different x ray energy spectra for kV and MV imaging, it is of interest to determine to what extent it is possible to preserve the benefits of kV and MV imaging using a single imaging detector. In this paper, considerations for the design of such a dual energy imager are explored through examination of the performance of a variety of hypothetical AMFPIs incorporating x ray converters based on the segmented scintillator approach. The performance of such imagers is characterized through simulation modeling in terms of contrast, noise, and CNR for a contrast phantom using volumetric (CBCT) imaging, as well as modulation transfer function (MTF), Swank factor, and signal using planar imaging.

2. METHODS

2.A. Converter designs examined in the study

Each converter design consists of a 2D matrix of identical elements comprising rectangular cuboid-shaped, scintillating crystals optically isolated by 0.05 mm thick, polystyrene septal walls.[24] (Thus, as in Ref. 24, the elements in each converter are not focused toward the radiation source.) All designs employ BGO material with thicknesses ranging from 0.25 to 4 cm, and element-to-element pitches (referred to as converter pitches) ranging from 0.508 to 1.016 mm. BGO was chosen due to the promising performance exhibited by previous prototypes based on this material, which offers desirable properties such as high electron density, high refractive index, and high optical transparency.[19,21,23] The lower limit for thickness corresponds to a point where the QE for MV imaging is ~15%, representing a substantial improvement compared to that of conventional MV AMFPIs, whereas the 4 cm upper limit (for which the QE is ~80%) corresponds to a point beyond which the rate of improvement in QE as a function of thickness diminishes rapidly. The lower limit for pitch corresponds to a point below which the scintillator fill factor drops sharply (due to the volume occupied by the fixed septal wall thickness), while the upper limit roughly corresponds to a point beyond which the advantageous spatial resolution offered by kV imaging would be severely compromised. Note that the 1 mm copper plate commonly employed as a build-up layer in the converter of conventional portal imagers was eliminated to avoid the detrimental effect of filtering of low energy x rays that provide high contrast in kV imaging. (The performance of MV imaging systems operated in the absence of an overlying metal plate has been previously examined.)[35,36] Also note that a reflector with negligible radiation attenuation was introduced to provide desirable optical properties and was modeled in the simulation with a zero mass attenuation coefficient for traversing x rays. Two extreme cases for the reflector were examined: one with 100% absorptivity and 0% reflectivity (referred to as "black"), and the other with 0% absorptivity and 100% reflectivity (referred to as "mirror").

The AMFPI array was modeled as an ~1 mm thick barium-doped glass plate representing the array substrate,[37] while the
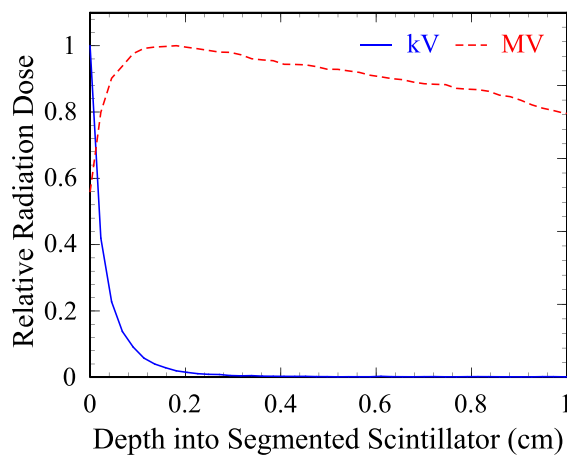
FIG. 1. Radiation dose profiles corresponding to 100 kVp (solid line) and 6 MV (dashed line) beam spectra along the depth of an ~1 cm thick BGO converter, obtained using the same Monte Carlo simulation techniques described in Sec. 2.B.1. The dose values for each spectrum have been normalized to unity at their respective maxima. Note that, whereas the kV profile exhibits a sharp decrease with depth, the MV profile follows the familiar pattern associated with the depth-dose distribution for a treatment beam (Ref. 39).

~1 μm thick pixel circuitry fabricated on the substrate was ignored due to its negligible effect on radiation attenuation. The array was coupled to the side of the converter opposite to that where the reflector resides. In the model, a value of 58% was used for the optical coupling efficiency of the photodiode[38] for light emitted by BGO. Throughout the study, the pixel pitch of the array was assumed to be the same as the converter pitch.

In addition to the two reflector types, the positioning of the array and the reflector relative to the x ray source was also varied. In this paper, the side of the converter facing the x ray source is referred to as the *entrance* surface while the other side is referred to as the *exit* surface. Under kV imaging conditions, dose drops quickly with depth into the converter from the entrance surface, with most of the radiation stopping in the first ~2 mm while, for an MV beam, dose is deposited more evenly throughout the thickness of the converter—as illustrated in Fig. 1. This significant difference in dose deposition requires careful design of the converter to preserve the respective benefits of both kV and MV imaging. Since energy deposition for kV photons is concentrated near the entrance surface, a conventional *front illumination* configuration, where the array is coupled to the exit surface and the reflector to the entrance surface as illustrated in Fig. 2(a), would lead to significant lateral spread of those optical photons reaching the array. This lateral spread, which is a consequence of imperfections in the optical isolation between neighboring scintillator elements, results in degradation of spatial resolution—an effect which increases for progressively thicker converter designs.

One possible means to reduce this loss of spatial resolution is through the use of a *rear illumination* configuration[40,41] in which the array is coupled to the entrance surface and the reflector to the exit surface of the converter, as shown in Fig. 2(b). In this configuration, for kV imaging, the majority of the optical photons generated in the direction of the
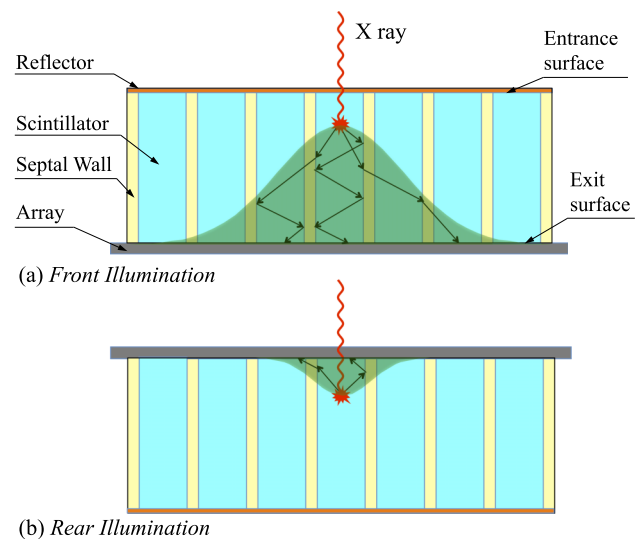

FIG. 2. Schematic, cutaway diagrams of imagers based on converters employing a segmented scintillator illustrating (a) front and (b) rear illumination configurations. The transparent bell-shaped regions superimposed on the diagrams signify the approximate lateral spread of optical photons reaching the array under kV imaging conditions. The arrows appearing in these regions correspond to examples of possible trajectories of optical light photons reaching the array.

array traverse much shorter distances before being detected, thereby reducing lateral optical spread and preserving spatial resolution of the imager. In the case of MV imaging, there is a parallel, though much reduced, benefit—due to the more uniform distribution of absorbed energy across the scintillator, as illustrated in Fig. 1.

For each converter of a certain thickness and pitch, a total of four configurations were explored: front illumination with a black reflector (referred to as "front-black"), front illumination with a mirror reflector ("front-mirror"), rear illumination with a black reflector ("rear-black"), and rear illumination with a mirror reflector ("rear-mirror").

2.B. Simulation framework

To characterize the MTF and CNR of the imager, a Monte Carlo-based hybrid modeling technique reported in a previous study was employed.[24] In addition, the effect of electronic additive noise was introduced through an analytical circuit noise model. A flowchart illustrating the major implementation steps of this coupled framework is shown in Fig. 3 and is described below.

2.B.1. Hybrid model

Radiation transport of x rays and optical transport of optical photons generated inside the scintillator were simulated using a hybrid modeling technique which decouples radiation and optical transport simulations and condenses the more computationally expensive optical simulation part into a single optical simulation per converter design. The technique, diagrammatically summarized on the left of Fig. 3, entails a sequential process where radiation images (obtained from
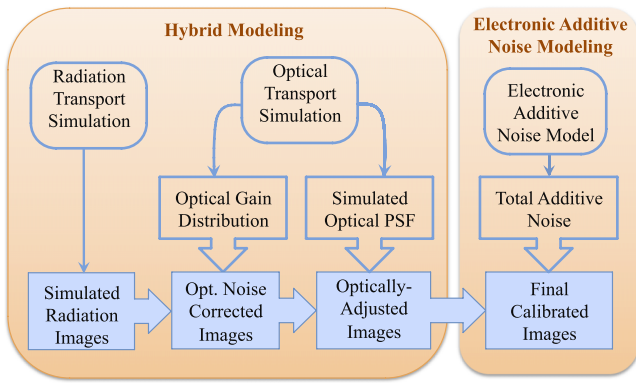
FIG. 3. Flowchart illustrating the simulation framework consisting of hybrid modeling (box on the left) and electronic additive noise modeling (box on the right) used in the study.

radiation transport simulations) are corrected with an optical gain distribution and optical point spread function (PSF) (both obtained from optical transport simulations) to account for optical Swank noise and optical blur, respectively.[24]

Monte Carlo radiation transport simulations were performed using the EGSnrc code,[42] with the geometries of the converters and the contrast phantom modeled using the EGSnrc C++ class library (egspp)[43] and with the egspp user code (as well as the input file that defines the geometry) modified as necessary. The parameter settings and algorithm options in the code that were employed in the study follow those used in previous theoretical investigations.[19,24] Both kV and MV simulations employed a point source located 130 cm away from the entrance surface of the converter. The kV spectrum corresponds to that of the 100 kVp "standard head" protocol of a Varian On-Board Imager (OBI) and was described using the TASMIP model,[44] with the tube voltage set to 100 kV and the intrinsic filtration set to 1.45 mm aluminum. A 6 MV spectrum corresponding to that of a Varian radiotherapy linear accelerator was adopted for MV simulations.[45]

The optical transport simulations were performed using the GEANT4 package.[46] The details and validation of the optical model, as well as the values for the associated optical parameters (which were obtained from a prototype segmented scintillator), appear in Ref. 24.

Both the radiation and optical transport Monte Carlo simulations were performed on a 64-bit Linux cluster with ~1000 processor cores (4.0 GHz AMD FX series). The study required a total of ~3.04×10^6 CPU hours, with a large majority of the time spent on the radiation transport simulations.

2.B.2. Electronic additive noise model

An analytical noise model was employed to account for the effect of electronic additive noise. The symbols in the following equations and the values of related parameters are summarized in Table I. The model takes into account the two dominant components of additive noise, reset noise associated with the thermal noise of the TFTs in the array pixels ($\sigma_{\text{TFT-thermal}}$) and noise of the external preamplifier electronics (σ_{amp}). The TFT reset thermal noise can be calculated from[47]

$$\sigma_{\text{TFT-thermal}} = \frac{1}{q}\sqrt{2k_B T C_{\text{pd}}}\,(e^-), \tag{1}$$

where q is the electron charge, k_B is the Boltzmann Constant, T is the room temperature in Kelvin, and C_{pd} is the photodiode capacitance of each array pixel. Following the parallel-plate capacitor model, the photodiode capacitance can be calculated from[48]

$$C_{\text{pd}} = \varepsilon_0 \varepsilon_{\text{Si}} \frac{A_{\text{pd}}}{d} = \varepsilon_0 \varepsilon_{\text{Si}} \frac{\eta a_{\text{pix}}^2}{d}, \tag{2}$$

where ε_0 is the vacuum permittivity, ε_{Si} is the relative static permittivity of silicon, A_{pd} is the area of the photodiode in each pixel, η is the optical fill factor of the array pixels, a_{pix} is the pixel pitch of the array, and d is the thickness of the photodiode. The array fill factor is assumed to be 100% [i.e., $\eta = 1.0$ in Eq. (2)]—given the relatively large pixel

TABLE I. Symbols, definitions, and values of the fixed parameters used in the electronic additive noise model. Note that the value used for photodiode thickness, d, corresponds to that of a modern array design (M13) (Ref. 49).

Symbols	Definitions	Values
$\sigma_{\text{TFT-thermal}}$	TFT reset thermal noise	
σ_{amp}	Preamplifier noise	
σ_{total}	Total additive noise	
C_{data}	Data line capacitance	115 pF
C_{pd}	Photodiode capacitance	
A_{pd}	Photodiode area	
a_{pix}	Array pixel pitch	
d	a-Si layer thickness in photodiode	1.50 μm
ε_{Si}	Relative static permittivity of silicon	12
ε_0	Vacuum permittivity	8.85×10^{-12} F/m
η	Array optical fill factor	1.0
q	Electron charge	1.60×10^{-19} C/e
k_B	Boltzmann constant	1.38×10^{-23} m^{2}kg/(s^{2}K)
T	Room temperature	295 K

pitches considered in the study.[49] The preamplifier noise was estimated using an expression based on the characteristics of a high performance preamplifier,[50]

$$\sigma_{\mathrm{amp}} = 15C_{\mathrm{data}} + 285 (e^-). \qquad (3)$$

In this equation, the value of the data line capacitance (C_{data}) was conservatively estimated using the capacitance per unit length of an array with a large pixel pitch,[47] scaled to the data line length of typical MV AMFPIs (i.e., 40 cm).

The total additive noise, σ_{total}, was calculated using

$$\sigma_{\mathrm{total}} = \sqrt{\sigma^2_{\mathrm{TFT\text{-}thermal}} + \sigma^2_{\mathrm{amp}}} (e^-). \qquad (4)$$

For each pitch examined in the study, a Gaussian distribution with zero mean and variance of σ_{total} was formed. For each pixel of the optically adjusted images obtained from the hybrid modeling technique, the additive noise was introduced through random sampling according to that distribution, resulting in additive noise calibrated images, as indicated in Fig. 3.

2.C. Determination of CBCT imaging metrics

For the radiation transport simulation of CBCT imaging, a contrast phantom with dimensions, composition, and inserts similar to those of a phantom used in a previous empirical study[21] was simulated under both kV and MV imaging conditions. The phantom consists of an 11.4 cm diameter, solid water cylinder with three 2.8 cm diameter, cylindrical tissue-equivalent inserts, all with a common length of 6 cm. Consistent with earlier studies,[21,24] the center of the phantom was positioned 124.2 cm from the source—thereby leaving a 1 mm gap between the converter and the bottom of the phantom. The inserts correspond to breast, solid water, and brain with electron densities of 0.954, 0.988, and 1.049 relative to water, respectively.[24] All converter designs have a detection area of $\sim 70 \times 140$ mm^2, resulting in matrix formats of 141×281, 95×189, and 71×141 for the examined pitches of 0.508, 0.762, and 1.016 mm, respectively. This converter area was chosen so as to be sufficiently large to allow imaging of the phantom. For a given converter design, imager configuration, and imaging condition, 180 projection radiation images were obtained by scanning the phantom tomographically at 2° angular increment over 360°. In the simulations, the x ray fluence incident on the phantom per tomographic scan corresponded to 1.14×10^8 and 4.32×10^7 x rays/mm^2 at 130 cm from the source for kV and MV CBCT, respectively. The kV fluence provides a dose equivalent to the 145 mAs standard head protocol for the Varian OBI kV CBCT imaging system, while the MV fluence provides a dose equivalent to that used in a previous empirical MV CBCT study (corresponding to a minimum of one beam pulse per projection).[21] In addition, for each converter design, imager configuration, and imaging condition, a set of 180 radiation flood images was obtained in the absence of the phantom, each using the same fluence as that used for the individual projection images of the phantom. Due to the distinctively different characteristics of the kV and MV dose

profiles, a weighted central slice CT dose index (CTDI$_W$) was used as a surrogate for imaging dose for kV and MV CBCT in order to facilitate comparisons between the kV and MV CBCT image doses used in the study. CTDI$_W$ is defined as[51]

$$\mathrm{CTDI}_W = \frac{1}{3} \sum D_C + \frac{2}{3} \sum D_P, \qquad (5)$$

where the doses at two landmark locations, the center (D_C) and the periphery (D_P, defined at 1 cm inside the phantom surface), are summed over all projection angles in the tomographic scan. Based on this definition, the fluence values used in kV and MV CBCT simulations correspond to CTDI$_W$ values of ~0.91 and ~3.0 cGy, respectively.

For the optical transport simulation, the segmented scintillator in each converter design took the form of a matrix of 101×101 elements. For each design, 10 000 simulation runs, each consisting of 10 000 optical photon histories, were performed. All photons were generated in the central element of the matrix, following the 3D radiation energy deposition profile of the corresponding converter design. The optical gain distribution and optical PSF obtained from this simulation were applied to the simulated radiation images to yield optically adjusted images, which accounted for the effect of both optical Swank noise and optical blur.[24] The optically adjusted images were then corrected for additive noise of the corresponding design to generate the final calibrated images.

A Feldkamp-based algorithm employing a ramp filter was used to reconstruct the volumetric images corresponding to the contrast phantom from a combination of the calibrated projection images and the average of the 180 calibrated flood images. The voxel pitch and single slice thickness used in the reconstruction were chosen to be equal to the converter pitch for each design. A suitable number of the reconstructed slices were binned to generate a slice thickness of ~5 mm, followed by a cupping artifact correction to remove the background trend caused by beam hardening.[21]

The CBCT performance of various converter designs was characterized in terms of contrast (*Contrast*), noise (*Noise*), and CNR of the tissue-equivalent inserts relative to the water-equivalent background in the reconstructed phantom images.[18] *Contrast* for a given insert was calculated in Hounsfield units (HU) using the equation

$$\mathrm{Contrast} = \frac{S_{\mathrm{obj}} - S_{\mathrm{water}}}{S_{\mathrm{water}}} \times 1000 \, (\mathrm{HU}), \qquad (6)$$

where S_{obj} and S_{water} represent the mean signal in the insert and water-equivalent background, respectively. Each signal was taken from a circular region with an ~14.2 mm diameter that excluded the edges of the inserts and the phantom. *Noise* was calculated using the equation

$$\mathrm{Noise} = \frac{\sigma_{\mathrm{obj}}}{S_{\mathrm{water}}} \times 1000 \, (\mathrm{HU}), \qquad (7)$$

where σ_{obj} represents the standard deviation of the signal in the insert. Finally, CNR was calculated from

$$\text{CNR} = \frac{S_{\text{obj}} - S_{\text{water}}}{\sigma_{\text{obj}}}. \tag{8}$$

2.D. Determination of imager MTF

The spatial resolution for each converter design was characterized in terms of the presampled MTF using the angled slit technique.[52] The radiation and optical transport simulations of MTF followed the steps described in a previous study,[24] generating an optically adjusted slit image for each design. Additive noise was subsequently included to yield a final calibrated slit image. This image was used to determine an oversampled line spread function, the 1D Fourier transform of which yielded the MTF.

2.E. Determination of Swank factor and signal

The steps used to determine Swank factor and signal (accounting for contributions of both radiation and optical effects) largely followed those reported in Ref. 20. (Swank factor is a metric with values ranging from 0 to 1, where higher values correspond to lower Swank noise.[53]) For each imager configuration and converter design, radiation transport simulation was performed using the EGSnrc code package, yielding a phase space file containing information for each energy deposition event within the converter for each interacting x ray. Using this phase space file, simulation of optical transport was subsequently performed using the GEANT4 code package to tally the number of optical photons detected for each x ray in the form of a pulse height distribution. The Swank factor I and signal S were calculated using the equations[53]

$$I = \frac{M_1^2}{M_0 M_2}, \tag{9}$$

$$S = \frac{M_1}{M_0}, \tag{10}$$

where M_i is the ith order moment of the pulse height distribution, $P(x)$, obtained from

$$M_i = \sum_k x_k^i P(x_k). \tag{11}$$

3. RESULTS

3.A. Comparison of imager configurations

A comparison of the relative merits of the four imager configurations described in Sec. 2.A was performed through characterization of their MTF, Swank factor, and signal performance under kV and MV imaging conditions. Figures 4–7 show results for the full range of converter thicknesses (0.25–4.0 cm) at a selected pitch of 1.016 mm—the same pitch as that of a prototype BGO segmented scintillator reported in a previous empirical study.[21]

Figure 4 shows the kV MTF results for the different imager configurations. As expected, the rear illumination results, shown in Figs. 4(b) and 4(d), exhibit systematically higher MTF compared to that for the corresponding front illumination cases shown in Figs. 4(a) and 4(c). This is a consequence of reduced lateral optical spread for rear illumination, as schematically illustrated in Fig. 2. Note that, for all but the *rear-mirror* configuration, MTF improves with decreasing converter thickness due to reduced scatter of primary x rays and lateral spread of optical photons. However, for the *rear-mirror* configuration [Fig. 4(b)], the MTF generally degrades with decreasing thickness. This reversed behavior originates from the increasing fraction of optical photons that are reflected by the mirror reflector and reach the array as thickness decreases. Such photons tend to undergo more interactions with the septal walls, leading to more lateral spread which, in turn, results in deterioration of spatial resolution. The absence of such photons for the *rear-black* configuration results in systematically higher MTF compared to that for the *rear-mirror* configuration. In addition, for the *rear-black* configuration, the MTF curves are closely clustered and relatively insensitive to changes in converter thickness, allowing for the possibility of using a greater thickness to achieve higher detection efficiency in MV imaging without substantial degradation of kV spatial resolution.

As is apparent in Fig. 5(a), under kV conditions, the rear illumination configurations (open symbols) provide better Swank factor than their front illumination counterparts (solid symbols). In addition, for a given converter thickness, *rear-black* and *rear-mirror* exhibit nearly identical Swank factors. The rear illumination configurations also provide generally higher signal than their front illumination counterparts, as shown in Fig. 5(b). For all but the *rear-black* configuration, signal decreases with thickness due to the increased number of absorbed photons along a longer mean optical path length. However, for the *rear-black* configuration, signal is relatively independent of converter thickness—largely as a result of the negligible contribution from optical photons generated in material beyond ∼0.25 cm. It is interesting to note that, for configurations with the same type (i.e., *mirror* or *black*) but different positioning of reflector (i.e., *front* and *rear*), signal values generally converge at smaller thicknesses—due to similarities in the mean optical path lengths for front and rear illuminations. This similarity results from a relatively more uniform energy deposition, and therefore more uniform generation of optical photons, throughout the converter thickness for thinner converters. Conversely, for configurations with the same reflector positioning but different reflector types, signal values converge at larger thicknesses due to the diminished importance of reflector type, resulting from reduced numbers of photons reaching the reflector. For example, for the two rear illumination configurations, although *rear-black* provides lower signal values than *rear-mirror* at smaller thicknesses, this signal difference quickly diminishes as thickness increases, resulting in a relative difference of only ∼2% at 2 cm and a negligible difference at 4 cm. Since a greater thickness is advantageous for improved
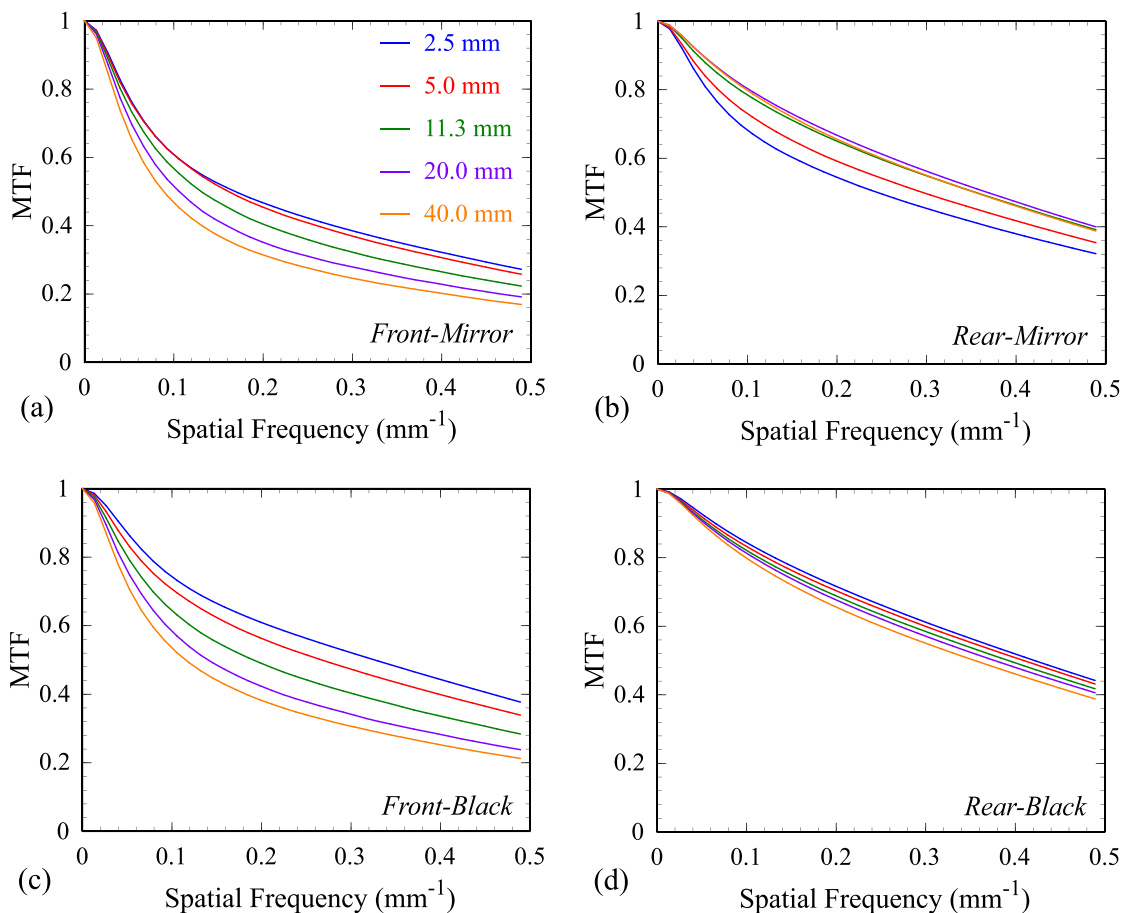
FIG. 4. MTF results under kV imaging conditions for 1.016 mm pitch imagers employing various converter thicknesses for the (a) *front-mirror*, (b) *rear-mirror*, (c) *front-black*, and (d) *rear-black* configurations.

quantum efficiency for MV imaging, the adoption of a black reflector is not expected to significantly constrain signal compared to the mirror reflector.

Figure 6 shows MV MTF results for the various imager configurations. In all cases, MTF performance is seen to improve with decreasing converter thickness. In addition, for a given thickness, the *rear-black* configuration is seen to provide equivalent or higher MTF compared with the other three configurations. Figure 7 shows that, as in the kV case, the rear illumination configurations provide generally better MV Swank factor and signal performance than their front illumination counterparts. In Fig. 7(b), while signal increases toward an asymptotic limit as thickness increases for rear illumination, largely due to asymptotically increasing QE, for front illumination signal initially increases and then decreases due to the competing effects of increasing QE and decreasing optical collection efficiency. Note that the signal results in Fig. 7(b) exhibit the same general trends of convergence observed in the kV case. Considering the two reflector types for rear illumination, although *rear-black* provides lower Swank factor and signal than *rear-mirror*, the differences are small for thick converters, with relative differences of only ~4% and 8% for Swank factor and signal, respectively, at a thickness of 2 cm, and negligible differences at 4 cm.

The results of the above analysis of MTF, Swank factor, and signal suggest that the *rear-black* configuration represents the most favorable design choice for a converter intended for kV and MV operation. This conclusion applies throughout the range of converter pitches considered in the study, the results for which (though not shown) exhibit trends similar to those at 1.016 mm. For that reason, only the *rear-black* configuration is considered in Secs. 3.B–3.D.

3.B. Comparison of converter designs

CNR performance for CBCT imaging under kV and MV imaging conditions as a function of converter thickness and pitch is shown in Fig. 8. For a given thickness and imaging condition, CNR consistently increases with pitch as a result of reduced noise due to more x ray quanta being detected by larger cross-sectional areas of scintillator elements. However, for a given pitch, the kV and MV behaviors of CNR as a function of thickness are distinctly different. In the case of kV and for a given pitch, CNR is relatively insensitive to changes in thickness [as seen in Fig. 8(a)]. This insensitivity is a consequence of the roughly constant level of QE under kV imaging conditions (ranging from ~94% to 99% for the thicknesses examined) as well as of the relative independence of MTF and Swank factor to changes in thickness (as
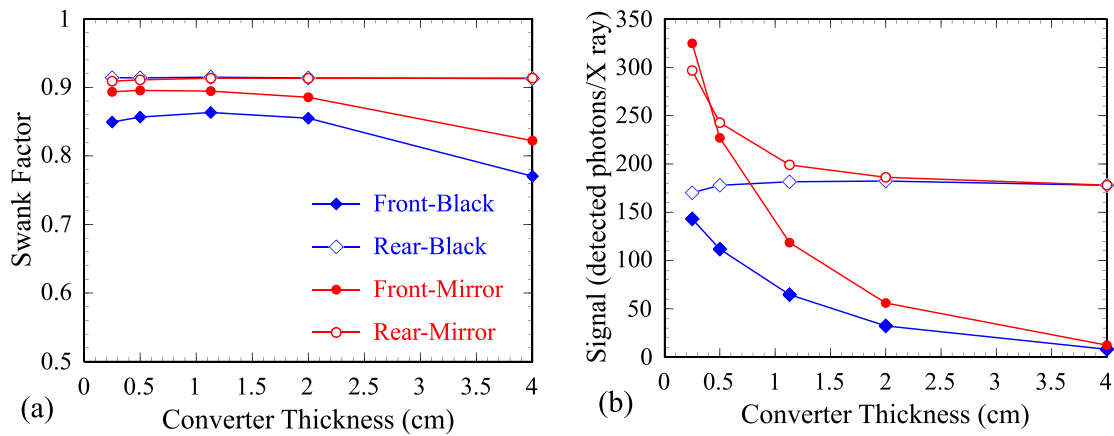
FIG. 5. Kilovoltage results for (a) Swank factor and (b) signal (defined as the average number of detected optical photons per interacting x ray) as a function of converter thickness for 1.016 mm pitch imagers.

described in Sec. 3.A). By comparison, in the case of MV and for a given pitch, the value of CNR increases with thickness [as seen in Fig. 8(b)] due to the significant increase in QE from ~15% to 80% for the thicknesses examined. Note that the increase in CNR exhibits an asymptotic behavior due to diminishing improvement in QE from increased converter thickness. For example, at a pitch of 0.508 mm, while CNR increases by ~32% from 1 to 2 cm, the increase is only ~9% from 2 to 4 cm.

It is clear that the identification of a single segmented scintillator converter design which exhibits performance that fulfills the needs of both kV and MV imaging is hindered by an inherent incompatibility. Specifically, MV imaging favors thicker converter designs with larger pitch so as to
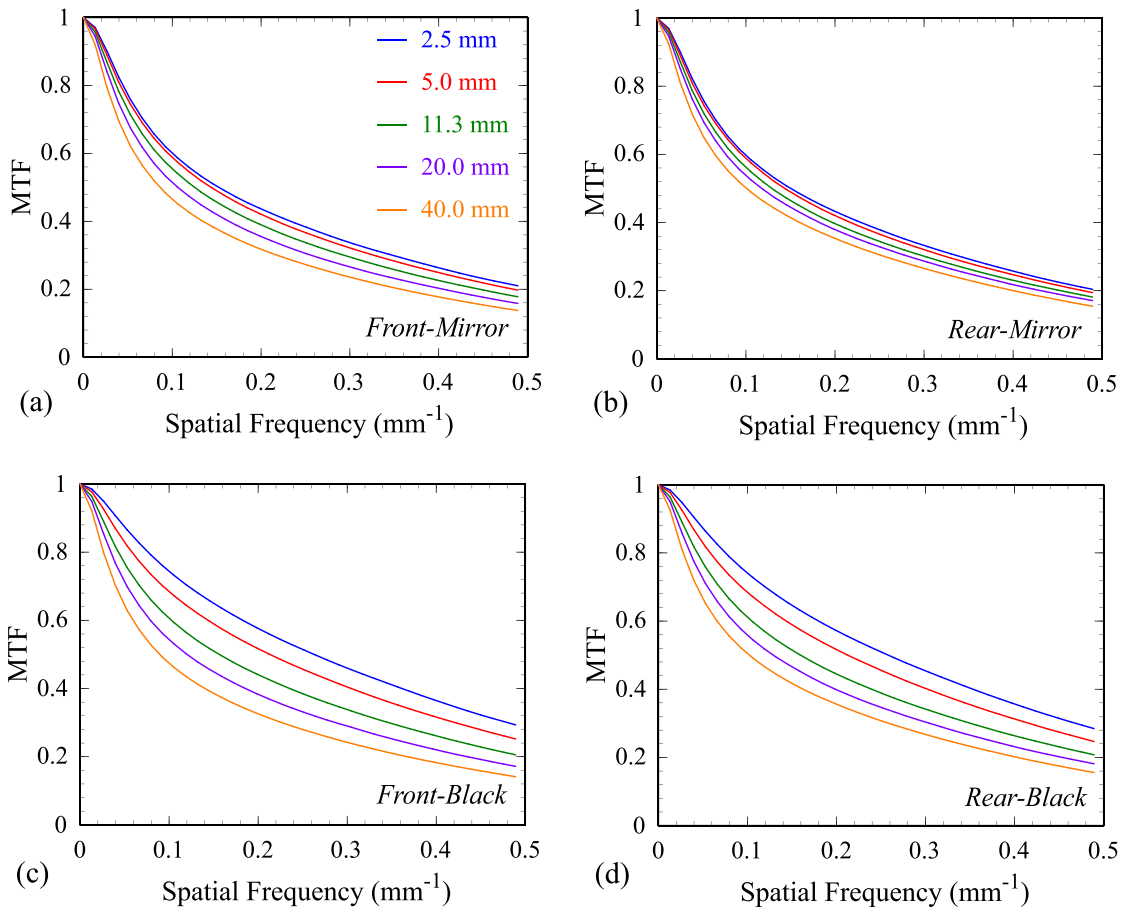

FIG. 6. MTF results under MV imaging conditions for 1.016 mm pitch imagers employing various converter thicknesses for the (a) *front-mirror*, (b) *rear-mirror*, (c) *front-black*, and (d) *rear-black* configurations.
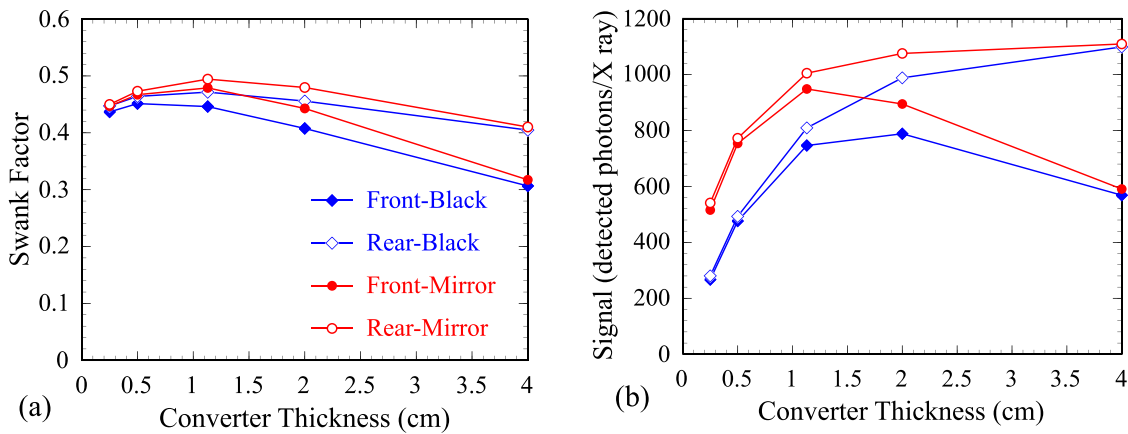
FIG. 7. MV results for (a) Swank factor and (b) signal as a function of converter thickness for 1.016 mm pitch imagers.

achieve higher CNR performance,[24] whereas kV imaging favors smaller pitch to maintain higher MTF performance, while being relatively insensitive to the choice of thickness. For that reason, a converter thickness of ~2 cm would be a favorable choice given the rapidly diminishing returns on MV CNR beyond this thickness, coupled with considerations of increasing material cost and difficulty of manufacture for thicker scintillators. Moreover, within the bounds of the current study, the preferred converter pitches for kV and MV imaging are 0.508 and 1.016 mm, respectively. This difference could be reconciled either through selection of a common intermediate pitch (e.g., 0.762 mm) or through selection of the smaller pitch in combination with the use of binning for MV (but not for kV) operation, as explored in Sec. 3.C.

3.C. Comparison of pitch-binning combinations

In this section, additive noise, MV CNR, and MTF performance are examined for the various combinations of converter pitches and binning modes. For pitches of 0.508, 0.762, and 1.016 mm with 1×1 binning (i.e., full resolution readout with

no binning), the corresponding sampling pitches are 0.508, 0.762, and 1.016 mm—which are denoted as $508_{1\times1}$, $762_{1\times1}$, and $1016_{1\times1}$, respectively. For a pitch of 0.508 mm with 2×2 binning, the corresponding sampling pitch is 1.016 mm and is denoted as $508_{2\times2}$. Values for TFT reset thermal noise, preamplifier noise, and total additive noise used in the CNR calculations for the different pitch-binning combinations are summarized in Table II.

Figure 9 shows the MV CNR performance for designs incorporating the various pitch-binning combinations. For the three combinations with no binning, CNR increases with converter pitch for a given thickness and increases with converter thickness for a given pitch—in both cases due to increased numbers of detected x ray quanta per scintillator element. For all converter thicknesses, $508_{2\times2}$ exhibits systematically lower (~15%–21%) CNR compared to that of $1016_{1\times1}$, despite having identical sampling pitch. This is primarily a consequence of two contributing factors—increased Swank noise due to a larger aspect ratio for the scintillator elements[20] and reduced QE due to the displacement of BGO crystal by more septal wall material. However, $508_{2\times2}$ exhibits systematically higher (~21%–31%)
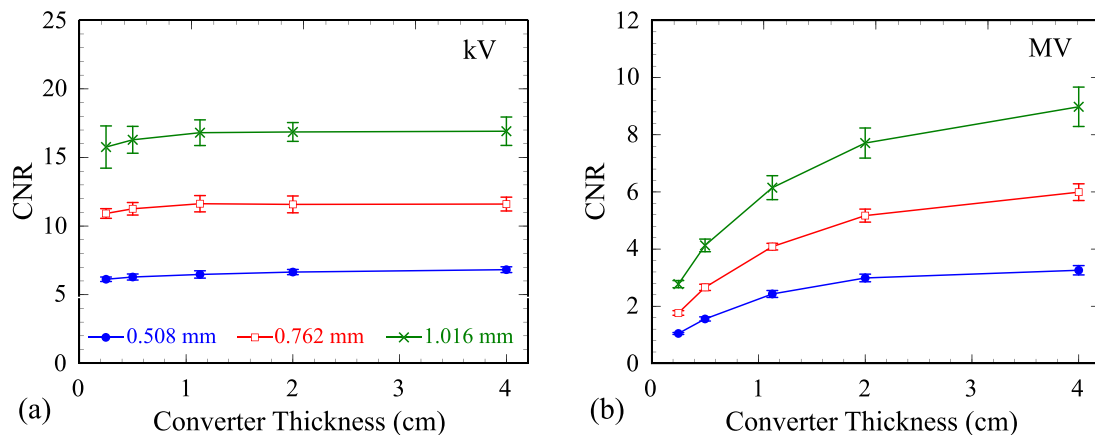

FIG. 8. Absolute value of CNR as a function of converter thickness and pitch for a phantom insert with a relative electron density of 0.954. The results were obtained using imager designs with the *rear-black* configuration and pitches ranging from 0.508 to 1.016 mm under (a) kV conditions with a CTDI$_W$ of ~0.91 cGy and (b) MV conditions with a CTDI$_W$ of ~3.0 cGy.

TABLE II. Estimates of the TFT reset thermal noise $\sigma_{\text{TFT-thermal}}$, preamplifier noise σ_{amp}, and the total additive noise σ_{total} of the various pitch-binning combinations calculated using Eqs. (1), (3), and (4). Note that values of σ_{amp} for $508_{2\times2}$ assume a postacquisition (i.e., purely digital) binning.

Pitch-binning combination	$508_{1\times1}$	$762_{1\times1}$	$1016_{1\times1}$	$508_{2\times2}$
Converter pitch (mm)	0.508	0.762	1.016	0.508
Sampling pitch (mm)	0.508	0.762	1.016	1.016
$\sigma_{\text{TFT-thermal}}$ (e^- [rms])	2408	3611	4816	4816
σ_{amp} (e^- [rms])	2010	2010	2010	4020
σ_{total} (e^- [rms])	3137	4133	5219	6273

CNR compared to $762_{1\times1}$—largely as a result of increased numbers of sampled x ray quanta.

Figure 10 shows the MV MTF performance for 2 cm thick converters corresponding to various pitch-binning combinations. As a result of binning, the MTF for $508_{2\times2}$ falls off more rapidly with spatial frequency compared to the MTF for $508_{1\times1}$, resulting in a relative difference of ~25% at a frequency of 0.49 mm^{-1} (the Nyquist frequency for a sampling pitch of 1.016 mm). However, despite having the same sampling pitch, the MTF for $508_{2\times2}$ is systematically higher than that for $1016_{1\times1}$ almost up to the Nyquist frequency, due to more constrained optical lateral spread as a result of more septal wall material in the path of optical photons for the former combination. Note that $762_{1\times1}$ and $508_{2\times2}$ demonstrate somewhat comparable MTF, with the former and latter combinations exhibiting slightly better performance at spatial frequencies above and below ~0.26 mm^{-1}, respectively.

In light of the various findings reported above, and under the assumptions of the current study, our results suggest that the most advantageous design for a dual energy imager based on BGO would incorporate a converter with a 0.508 mm pitch and 2 cm thickness, operated using the rear-illumination configuration and coupled to a black reflector. The imager should be operated at full resolution for kV imaging (i.e., $508_{1\times1}$) and 2×2 binning mode for MV imaging

(i.e., $508_{2\times2}$). An example of the CBCT performance of such an imager is provided in Sec. 3.D.

3.D. Performance of the proposed dual energy imager

Reconstructed CBCT images of the contrast phantom obtained from imagers incorporating various converter designs are shown in Fig. 11. Figures 11(a) and 11(b) show simulated MV and kV CBCT images acquired from the proposed BGO-based dual energy imager (referred to as the BGO imager) corresponding to pitch-binning combinations of $508_{2\times2}$ and $508_{1\times1}$, respectively. Compared with the MV image (obtained at ~3.0 cGy), the kV image exhibits superior soft-tissue visualization by virtue of better CNR performance, despite the use of a much smaller dose of ~0.91 cGy—a result of higher contrast and lower noise under kV conditions. It is of interest to note that, for the insert in the lower left of each image, the gray scale relative to the background is reversed between the kV and MV images. This is likely a result of the specific chemical composition of that insert, combined with the difference in the dominant x ray interaction mechanisms and their behaviors under kV and MV imaging conditions: the photoelectric effect under kV conditions, which scales with the fourth power of electron density; and the Compton effect under MV conditions, which scales linearly with electron density. For purposes of comparison, Fig. 11(c)
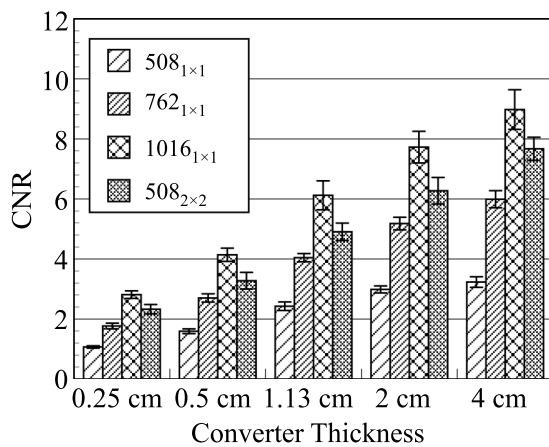

FIG. 9. Absolute value of CNR under MV imaging conditions as a function of converter thickness for a phantom insert with a relative electron density of 0.954. These results were obtained using converters corresponding to various pitch-binning combinations.
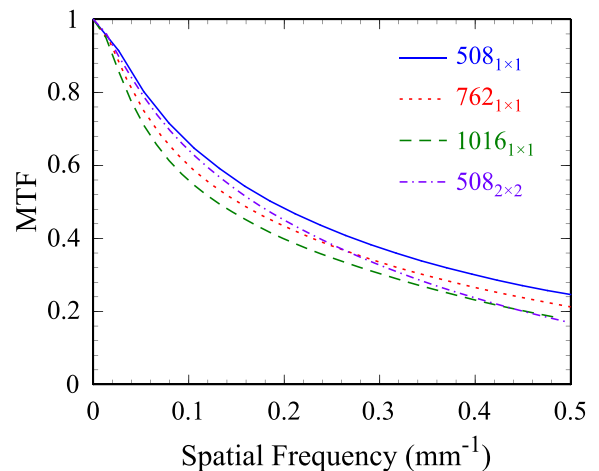

FIG. 10. MV MTF results for 2 cm thick converters corresponding to various pitch-binning combinations.
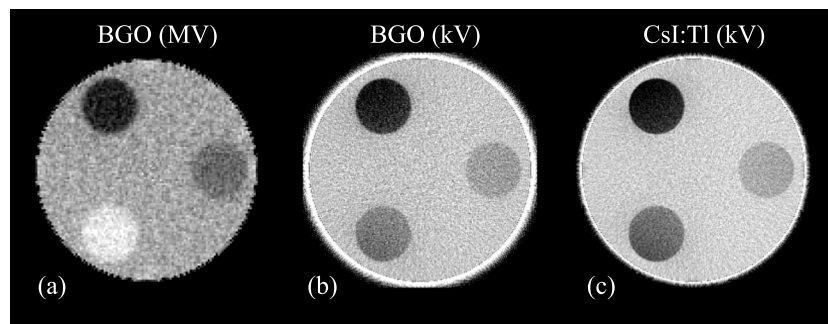
FIG. 11. Reconstructed CBCT images obtained from a simulated imager based on a 2 cm thick BGO converter and corresponding to pitch-binning combinations of (a) $508_{2\times2}$ at 6 MV, and (b) $508_{1\times1}$ at 100 kVp. Also shown for purpose of comparison is (c) a CBCT image obtained under 100 kVp from a simulated imager based on a 600 μm thick CsI:Tl converter. Note that the MV CBCT image was obtained at a CTDI$_W$ of ~3.0 cGy, while the kV CBCT images were obtained at a CTDI$_W$ of ~0.91 cGy. Also note that the relative electron densities of the inserts (clockwise from the top) are 0.954, 0.988 and 1.049.

shows a kV CBCT image for a simulated imager based on a 600 μm thick CsI:Tl converter (referred to as the CsI:Tl imager), representing the type of kV CBCT imagers used in radiotherapy treatment rooms. The simulation used the same general framework employed for the BGO imager, but with a value of 63% used for the optical coupling efficiency of the photodiode for light emitted by CsI:Tl. However, for the simulation of radiation effects, the columnar-structured CsI:Tl used in clinical imagers was approximated as a homogenous layer with a packing density of 75%.[54] For optical effects, optical spread was accounted for through use of the optical MTF deduced from the reported system MTF of a commercial kV imager based on CsI:Tl,[55] while optical Swank noise was neglected given that the Swank factor is close to unity under kV conditions.[54] Moreover, the same additive noise level as that used for the BGO imager simulations was assumed. The kV image obtained from the CsI:Tl imager [Fig. 11(c)] exhibits visual traits similar to those in the kV image obtained from the BGO imager [Fig. 11(b)]—except for a slight difference in contrast for the lower left insert. This difference is largely due to the difference in spectral response between CsI:Tl and BGO scintillator materials.

Quantitatively, CNR values extracted from the kV image obtained from the CsI:Tl imager [Fig. 11(c)] are higher than those extracted from the kV image obtained from the BGO imager [Fig. 11(b)] by ~22%–44% for the three inserts. For the BGO image, CNR performance was degraded as a result of the filtration of incident x rays by the 1 mm thick layer of glass substrate in the rear illumination configuration and by the detrimental effect of additive noise on CNR resulting from the relatively modest optical yield of the BGO material (~8000 photons/MeV deposited energy). By comparison, for the CsI:Tl image, there is no filtration effect (since rear illumination is not used) and the additive noise has negligible effect on CNR due to the much larger optical yield of CsI:Tl (~54 000 photons/MeV deposited energy).

Figure 12 shows simulated results for radiation MTF (obtained in the absence of optical effects) and system MTF, both obtained under kV imaging conditions for the BGO and CsI:Tl imagers. The imagers have nearly identical radiation MTFs, with the BGO imager exhibiting a slight advantage at higher frequencies (e.g., ~4% at the Nyquist frequency).

However, after the inclusion of optical effects, system MTF for the BGO imager is lower than that for the CsI:Tl imager. This difference is mainly due to the greater lateral spread of optical photons in the BGO converter, which is a consequence of the use of thicker scintillator material and the nonideal optical isolation of the septal walls.

4. DISCUSSION

In this study, theoretical modeling through Monte Carlo simulation has demonstrated that, through careful design, a single imager based on a thick, segmented BGO scintillator should be able to achieve soft tissue visualization at low, clinically practical doses by virtue of high QE for MV imaging, while helping to preserve the high spatial resolution and high contrast offered by kV imaging. Such a dual energy imager could facilitate simplification of current treatment room imaging systems and their associated quality assurance. In addition, such an imager operated in conjunction with a treatment machine offering coincident kV and MV FOVs
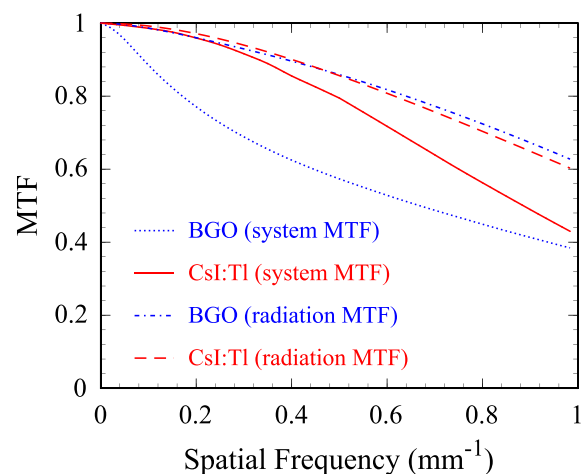

FIG. 12. Results for system MTF and radiation MTF obtained under kV irradiation conditions for the same simulated BGO and CsI:Tl imagers used to generate the images in Figs. 11(b) and 11(c), respectively.

could reduce geometric uncertainties and facilitate more precise integration of kV and MV imaging information.

Beyond the constraints and assumptions of the present study, a number of observations relating to the methodology used are as follows.

For converters with septal walls providing improved optical properties (i.e., increased and reduced septal wall reflectivity and absorption, respectively), it is anticipated that the *rear-black* configuration would remain the most favorable imaging configuration for a dual-energy (i.e., kV and MV) imager— although with a diminished relative advantage compared to the other configurations. For that configuration and with septal walls that provide improved optical isolation, MTF and CNR would increase and decrease, respectively—due to reduced lateral spread of optical photons.[24] While MTF and CNR would still be largely independent of converter thickness under kV conditions, for MV conditions, the increase in CNR as a function of converter thickness would be even less pronounced for thicknesses larger than ~2 cm,[24] thereby continuing to favor the choice of a thickness of ~2 cm.

The unfocused, rectangular cuboid-shaped crystals assumed in this study are subject to the effects of beam divergence. In the case of MV imaging, the effects of divergence on the reported results are limited by virtue of the relatively small detection area assumed in the study. For larger area detectors (e.g., 40×40 cm^2), MTF would be progressively more degraded for detector thicknesses greater than ~1 cm, while noise would not be affected[22,56]—leaving CNR unchanged. In the case of kV imaging, divergence effects are small due to the limited depth of x ray penetration into the crystal, combined with the relatively large pitch of the converters.

For imagers incorporating BGO converters, while the *rear-black* configuration generally provides superior performance compared to that of other configurations, under kV imaging conditions, CNR performance is expected to be lower than that of commercial kV CBCT systems employing CsI:Tl converters. This lower CNR performance can be partly attributed to the reversed position of the AMFPI array glass substrate, which causes filtration of the low energy component of the kV spectrum. (Such an effect is negligible under MV imaging conditions.) However, this detrimental effect could be mitigated through the use of a thinner substrate and/or a less dense substrate material such as plastic. In fact, flexible substrates made of plastic are under investigation for adoption into AMFPI array designs by virtue of their robustness compared to glass.[57]

The converter designs examined in this study are based on BGO, which has an optical yield of ~8000 photons/MeV of deposited energy. Due to this relatively low yield compared to that of other common inorganic scintillator materials, the performance of imagers incorporating BGO converters is more affected by additive noise, especially for kV imaging which utilizes much smaller doses than MV imaging, as reported in Sec. 3.D. Other scintillator materials with higher yield, such as CdWO$_4$ and LYSO (having yields of ~12 000–15 000 and ~32 000 photons/MeV of deposited energy, respectively), would be good candidates for minimizing the effect of additive noise in order to improve CNR—thus

helping to achieve quantum-limited behavior for both kV and MV imaging.

The methodology presented in this paper for investigating the design of an imager to be operated at both diagnostic and radiotherapy energies should be applicable to other dual imaging conditions as well. For example, given the recent availability of treatment machines offering an additional, relatively low MV x ray beam with a greater diagnostic spectral component to facilitate higher-contrast imaging,[31,32] the present methodology could help to guide the design of an imager that would provide the most advantageous combined performance with the treatment and imaging beams. Finally, the possibility of extending the current methodology to include consideration of dosimetric capabilities in imager design is of interest and is under investigation.

ACKNOWLEDGMENTS

a)Author to whom correspondence should be addressed. Electronic mail: antonuk@umich.edu; Telephone: 734-936-4312; Fax: 734-936-2261.

[1]L. E. Antonuk, "Electronic portal imaging devices: A review and historical perspective of contemporary technologies and research," Phys. Med. Biol. **47**, R31–R65 (2002).

[2]N. Mail, D. Moseley, J. Siewerdsen, and D. Jaffray, "The influence of bowtie filtration on cone-beam CT image quality," Med. Phys. **36**, 22–32 (2009).

[3]M. Aubin, O. Morin, J. Chen, A. Gillis, B. Pickett, J. Aubry, C. Akazawa, J. Speight, M. Roach III, and J. Pouliot, "The use of megavoltage cone-beam CT to complement CT for target definition in pelvic radiotherapy in the presence of hip replacement," Br. J. Radiol. **79**, 918–921 (2006).

[4]O. Morin, J. Chen, M. Aubin, A. Gillis, J.-F. Aubry, S. Bose, H. Chen, M. Descovich, P. Xia, and J. Pouliot, "Dose calculation using megavoltage cone-beam CT," Int. J. Radiat. Oncol., Biol., Phys. **67**, 1201–1210 (2007).

[5]Y. El-Mohri, K.-W. Jee, L. E. Antonuk, M. Maolinbay, and Q. Zhao, "Determination of the detective quantum efficiency of a prototype, megavoltage indirect detection, active matrix flat-panel imager," Med. Phys. **28**, 2538–2550 (2001); Erratum: Med. Phys. **33**, 251 (2006).

[6]B. A. Groh, J. H. Siewerdsen, D. G. Drake, J. W. Wong, and D. A. Jaffray, "A performance comparison of flat-panel imager-based MV and kV cone-beam CT," Med. Phys. **29**, 967–975 (2002).

[7]E. C. Ford, J. Chang, K. Mueller, K. Sidhu, D. Todor, G. Mageras, E. Yorke, C. C. Ling, and H. Amols, "Cone-beam CT with megavoltage beams and an amorphous silicon electronic portal imaging device: Potential for verification of radiotherapy of lung cancer," Med. Phys. **29**, 2913–2924 (2002).

[8]T. R. Mackie, "History of tomotherapy," Phys. Med. Biol. **51**, R427–R453 (2006).

[9]H. Keller, M. Glass, R. Hinderer, K. Ruchala, R. Jeraj, G. Olivera, and T. R. Mackie, "Monte Carlo study of a highly efficient gas ionization detector for megavoltage imaging and image-guided radiotherapy," Med. Phys. **29**, 165–175 (2002).

[10]S. Rathee, D. Tu, T. T. Monajemi, D. W. Rickey, and B. G. Fallone, "A bench-top megavoltage fan-beam CT using CdWO4-photodiode detectors. I. System description and detector characterization," Med. Phys. **33**, 1078–1089 (2006).

[11]S. S. Samant and A. Gopal, "Analysis of the kinestatic charge detection system as a high detective quantum efficiency electronic portal imaging device," Med. Phys. **33**, 3557–3567 (2006).

[12]P. F. Kirvan, T. T. Monajemi, B. G. Fallone, and S. Rathee, "Performance characterization of a MVCT scanner using multislice thick, segmented cadmium tungstate-photodode detectors," Med. Phys. **37**, 249–257 (2010).

[13] M. A. Mosleh-Shirazi, P. M. Evans, W. Swindell, J. R. N. Symonds-Tayler, S. Webb, and M. Partridge, "Rapid portal imaging with a high-efficiency, large field-of-view detector," Med. Phys. **25**, 2333–2346 (1998).

[14] E. J. Seppi, P. Munro, S. W. Johnsen, E. G. Shapiro, C. Tognina, D. Jones, J. M. Pavkovich, C. Webb, I. Mollov, L. D. Partain, and R. E. Colbeth, "Megavoltage cone-beam computed tomography using a high-efficiency image receptor," Int. J. Radiat. Oncol., Biol., Phys. **55**, 793–803 (2003).

[15] A. Sawant, L. E. Antonuk, Y. El-Mohri, Y. Li, Z. Su, Y. Wang, J. Yamamoto, Q. Zhao, H. Du, and J. Daniel, "Segmented phosphors: Mems-based high quantum efficiency detectors for megavoltage x-ray imaging," Med. Phys. **32**, 553–565 (2005).

[16] E. K. Breitbach, J. S. Maltz, B. Gangadharan, A. Bani-Hashemi, C. M. Anderson, S. K. Bhatia, J. Stiles, D. S. Edwards, and R. T. Flynn, "Image quality improvement in megavoltage cone beam CT using an imaging beam line and a sintered pixelated array system," Med. Phys. **38**, 5969–5979 (2011).

[17] A. Sawant, L. E. Antonuk, Y. El-Mohri, Q. Zhao, Y. Wang, Y. Li, H. Du, and L. Perna, "Segmented crystalline scintillators: Empirical and theoretical investigation of a high quantum efficiency EPID based on an initial engineering prototype CsI(Tl) detector," Med. Phys. **33**, 1053–1066 (2006).

[18] Y. Wang, L. E. Antonuk, Y. El-Mohri, Q. Zhao, A. Sawant, and H. Du, "Monte Carlo investigations of megavoltage cone-beam CT using thick, segmented scintillating detectors for soft tissue visualization," Med. Phys. **35**, 145–158 (2008).

[19] Y. Wang, L. E. Antonuk, Q. Zhao, Y. El-Mohri, and L. Perna, "High-DQE EPIDs based on thick, segmented BGO and CsI: Tl scintillators: Performance evaluation at extremely low dose," Med. Phys. **36**, 5707–5718 (2009).

[20] Y. Wang, L. E. Antonuk, Y. El-Mohri, and Q. Zhao, "A Monte Carlo investigation of Swank noise for thick, segmented, crystalline scintillators for radiotherapy imaging," Med. Phys. **36**, 3227–3238 (2009).

[21] Y. El-Mohri, L. E. Antonuk, Q. Zhao, R. B. Choroszucha, H. Jiang, and L. Liu, "Low-dose megavoltage cone-beam CT imaging using thick, segmented scintillators," Phys. Med. Biol. **56**, 1509–1527 (2011).

[22] L. Liu, L. E. Antonuk, Q. Zhao, Y. El-Mohri, and H. Jiang, "Countering beam divergence effects with focused segmented scintillators for high DQE megavoltage active matrix imagers," Phys. Med. Biol. **57**, 5343–5358 (2012).

[23] Y. El-Mohri, L. E. Antonuk, R. B. Choroszucha, Q. Zhao, H. Jiang, and L. Liu, "Optimization of the performance of segmented scintillators for radiotherapy imaging through novel binning techniques," Phys. Med. Biol. **59**, 797–818 (2014).

[24] L. Liu, L. E. Antonuk, Y. El-Mohri, Q. Zhao, and H. Jiang, "Optimization of the design of thick, segmented scintillators for megavoltage cone-beam CT using a novel, hybrid modeling technique," Med. Phys. **41**, 061916 (14pp.) (2014).

[25] M. Weissbluth, C. Karzmark, R. Steele, and A. Selby, "The Stanford medical linear accelerator: II. Installation and physical measurements 1," Radiology **72**, 242–265 (1959).

[26] H. Johns and J. Cunningham, "A precision cobalt 60 unit for fixed field and rotation therapy," Am. J. Roentgenol., Radium Ther. Nucl. Med. **81**, 4–12 (1959).

[27] Y. Cho and P. Munro, "Kilovision: Thermal modeling of a kilovoltage x-ray source integrated into a medical linear accelerator," Med. Phys. **29**, 2101–2108 (2002).

[28] D. M. Galbraith, "Low-energy imaging with high-energy bremsstrahlung beams," Med. Phys. **16**, 734–746 (1989).

[29] B. A. Faddegon, V. Wu, J. Pouliot, B. Gangadharan, and A. Bani-Hashemi, "Low dose megavoltage cone beam computed tomography with an unflattened 4 MV beam from a carbon target," Med. Phys. **35**, 5777–5786 (2008).

[30] J. L. Robar, T. Connell, W. Huang, and R. G. Kelly, "Megavoltage planar and cone-beam imaging with low-Z targets: Dependence of image quality improvement on beam energy and patient separation," Med. Phys. **36**, 3955–3963 (2009).

[31] D. Roberts, V. Hansen, M. Thompson, G. Poludniowski, A. Niven, J. Seco, and P. Evans, "Kilovoltage energy imaging with a radiotherapy linac with a continuously variable energy range," Med. Phys. **39**, 1218–1226 (2012).

[32] D. Parsons, J. L. Robar, and D. Sawkey, "A Monte Carlo investigation of low-Z target image quality generated in a linear accelerator using varian's virtualinac," Med. Phys. **41**, 021719 (6pp.) (2014).

[33] J. Rottmann, M. Aristophanous, A. Chen, L. Court, and R. Berbeco, "A multi-region algorithm for markerless beam's-eye view lung tumor tracking," Phys. Med. Biol. **55**, 5585–5598 (2010).

[34] F.-F. Yin, H. Guan, and W. Lu, "A technique for on-board CT reconstruction using both kilovoltage and megavoltage beam projections for 3D treatment verification," Med. Phys. **32**, 2819–2826 (2005).

[35] T. Falco and B. G. Fallone, "Characteristics of metal-plate/film detectors at therapy energies. I. Modulation transfer function," Med. Phys. **25**, 2455–2462 (1998).

[36] C. Kausch, B. Schreiber, F. Kreuder, R. Schmidt, and O. Dössel, "Monte Carlo simulations of the imaging performance of metal plate/phosphor screens used in radiotherapy," Med. Phys. **26**, 2113–2124 (1999).

[37] J. Yorkston, L. E. Antonuk, Y. El-Mohri, K.-W. Jee, W. Huang, M. Maolinbay, X. Rong, J. H. Siewerdsen, and D. P. Trauernicht, "Improved spatial resolution in flat-panel imaging systems," Proc. SPIE **3336**, 556–563 (1998).

[38] Y. El-Mohri, L. E. Antonuk, Q. Zhao, Y. Wang, Y. Li, H. Du, and A. Sawant, "Performance of a high fill factor, indirect detection prototype flat-panel imager for mammography," Med. Phys. **34**, 315–327 (2007).

[39] F. H. Attix, *Introduction to Radiological Physics and Radiation Dosimetry* (Wiley-VCH Verlag GmbH & Co., Weinheim, 2004).

[40] K. Sato, F. Nariyuki, H. Nomura, A. Takasu, S. Fukui, M. Nakatsu, Y. Okada, T. Nabeta, and Y. Hosoi, "Effect of x-ray incident direction and scintillator layer design on image quality of indirect-conversion flat-panel detector with GOS phosphor," Proc. SPIE **7961**, 79614I (2011).

[41] S. Rivetti, N. Lanconelli, M. Bertolini, A. Nitrosi, and A. Burani, "Characterization of a clinical unit for digital radiography based on irradiation side sampling technology," Med. Phys. **40**, 101902 (11pp.) (2013).

[42] I. Kawrakow and D. W. O. Rogers, "The EGSnrc code system: Monte carlo simulation of electron and photon transport," *Technical Report No. PIRS–701* (National Research Council of Canada, Ottawa, Canada, 2000).

[43] I. Kawrakow, "egspp: The EGSnrc c++ class library," *Technical Report No. PIRS-899* (National Research Council of Canada, Ottawa, Canada, 2005).

[44] J. M. Boone and J. A. Seibert, "An accurate method for computer-generating tungsten anode x-ray spectra from 30 to 140 kV," Med. Phys. **24**, 1661–1670 (1997).

[45] D. Sheikh-Bagheri, Ph.D. thesis, Carleton University, Ottawa, 1999.

[46] S. Agostinelli *et al.*, "GEANT4–A simulation toolkit," Nucl. Instrum. Methods Phys. Res., Sect. A **506**, 250–303 (2003).

[47] M. Maolinbay, Y. El-Mohri, L. Antonuk, K.-W. Jee, S. Nassif, X. Rong, and Q. Zhao, "Additive noise properties of active matrix flat-panel imagers," Med. Phys. **27**, 1841–1854 (2000).

[48] P. A. Tipler and G. Mosca, *Physics for Scientists and Engineers*, 6 ed. (Freeman, W. H. & Company, New York, NY, 2007).

[49] L. E. Antonuk, Q. Zhao, Y. El-Mohri, H. Du, Y. Wang, R. A. Street, J. Ho, R. Weisfield, and W. Yao, "An investigation of signal performance enhancements achieved through innovative pixel design across several generations of indirect detection, active matrix, flat-panel arrays," Med. Phys. **36**, 3322–3339 (2009).

[50] M. Maolinbay, T. Zimmerman, R. Yarema, L. Antonuk, Y. El-Mohri, and M. Yeakey, "Design and performance of a low noise, 128-channel ASIC preamplifier for readout of active matrix flat-panel imaging arrays," Nucl. Instrum. Methods Phys. Res., Sect. A **485**, 661–675 (2002).

[51] M. F. Fast, T. Koenig, U. Oelfke, and S. Nill, "Performance characteristics of a novel megavoltage cone-beam-computed tomography device," Phys. Med. Biol. **57**, N15–N24 (2012).

[52] H. Fujita, D. Tsai, T. Itoh, K. Doi, J. Morishita, K. Ueda, and A. Ohtsuka, "A simple method for determining the modulation transfer function in digital radiography," IEEE Trans. Med. Imaging **11**, 34–39 (1992).

[53] R. K. Swank, "Absorption and noise in x-ray phosphors," J. Appl. Phys. **44**, 4199–4203 (1973).

[54] W. Zhao, G. Ristic, and J. A. Rowlands, "X-ray imaging performance of structured cesium iodide scintillators," Med. Phys. **31**, 2594–2605 (2004).

[55] E. Samei, "Image quality in two phosphor-based flat panel digital radiographic detectors," Med. Phys. **30**, 1747–1757 (2003).

[56] Y. Wang, Y. El-Mohri, L. E. Antonuk, and Q. Zhao, "Monte Carlo investigations of the effect of beam divergence on thick, segmented crystalline scintillators for radiotherapy imaging," Phys. Med. Biol. **55**, 3659–3673 (2010).

[57] R. A. Street, W. S. Wong, and R. Lujan, "Curved electronic pixel arrays using a cut and bend approach," J. Appl. Phys. **105**, 104504 (2009).